



DESIGN AND TESTING OF SOUND SOURCES FOR PHASED MICROPHONE ARRAY CALIBRATION

S. Kroeber¹, K. Ehrenfried¹, L. Koop¹

¹ German Aerospace Center (DLR)
Bunsenstrasse 10, 37073 Goettingen, Germany
Email: stefan.kroeber@dlr.de

ABSTRACT

The phased array technique is a powerful tool for the localisation and quantification of sound sources in aeroacoustic testing. The accuracy of the results is limited due to phase and sensitivity errors of the microphones. A reliable calibration procedure for the microphone array would enhance the applicability of the measurement technique. Currently, appropriate sound sources are lacking, especially for in-flow calibration. An ideal calibration sound source exhibits monopole characteristics and covers a frequency range up to 70 kHz. The present study reviews concepts for omni-directional sound sources and evaluates their capability for microphone array calibration. Two concepts of calibration sources with aerodynamic fairings for the use in wind tunnels have been developed. The radiated sound field of both probes was examined in experiments in an anechoic facility. The presented results comprise the spatial amplitude characteristics of the designed sound sources. In addition, beamforming with a synthetic microphone array was performed to analyse the phase characteristics.

1 INTRODUCTION

The phased microphone array application finds use in a widely varying operative range. In many cases sound sources generated by common carriers are localized and quantified. The aeroacoustic testing is often carried out in closed wind tunnels using scaled models. This requires broad band measurements up to 70 kHz and more. Nowadays microphone arrays with several hundred sensors are used, which leads to the expenditure of a tremendous effort to eliminate sources of error. In spite of great care one has to expect deviations between actual and believed microphone positions, channel-to-channel phase differences in the measured data, microphone incidence effects, differences in the microphone sensitivities and array installation effects. In order to address this matter, Mueller [8] has proposed a calibration procedure for the microphone phase and amplitude calibration. Currently, however, it lacks an appropriate sound source to conduct successfully such a calibration also in the flow. Optimal would be an ideal monopole source that can emit sufficiently high sound pressure levels in the frequency range up to 70 kHz and has no disturbing influence on the flow field. Up until now it has been possible to achieve an omni-directional sound field for compact sources for low frequencies in the far field. However, there are ambitions to generate at least partially an omni-directional sound field for higher frequencies in the far field. In the following an overview of concepts for omni-directional sound sources is given.

2 OVERVIEW OF CONCEPTS FOR OMNI-DIRECTIONAL SOUND SOURCES

2.1 Electromechanic sound sources

A selection of electromechanic sound sources is shown in Fig. 1. Bang & Olufsen [1] employs an acoustic lens to guide the sound waves of a conventional dome loudspeaker. The result should segmentally correspond to an omni-directional sound field. MBL [7] offers a loudspeaker system that combines a subwoofer, midrange speaker and a tweeter. The particular membrane has the shape of a prolate solid of revolution and it alters its diameter through a contraction in longitudinal direction. The generated sound field should be similar to that of a breathing sphere. In general the hi-fi manufacturers do not provide any experimental results in order to prove the spherical-shaped sound field. Bruel & Kjaer [2] offers a DIN and ISO certified sound source for building acoustics with omni-directional sound radiation. Type 4292 generates the sound field through superposition of 12 loudspeakers arranged on a dodecahedron. It becomes apparent that the sound field directivity depends on frequency and is subject to sound pressure fluctuations up to 10 dB in the frequency range of 1 kHz to 8 kHz, as illustrated in Fig. 2. The source is not suited for a microphone array calibration. On the one hand the covered frequency range is too low and on the other an aerodynamic fairing for the sound source is fairly difficult to realize.

2.2 Aeroacoustic sound sources

Dobrzynski et al. [4] has developed an aeroacoustic sound source for the calibration of concave mirrors. The design solution incorporates a pneumatic source. Compressed air of 4 bar is used to generate 8 jets in an elliptic housing which is located in the wind tunnel flow.

The radiation takes place over a metal fabric covered orifice in the housing. The orifice diameter represents a compromise between minimal source size, coherent sound field and required sound pressure level. Suction helps to reduce the influence of the injected gas mass on the flow. According to Dobrzynski et al. [4] the designed sound source fulfills the requirements, but they do not give an experimental verification:

- small size to match the characteristics of a point source
- minimal influence of the aerodynamic fairing on the sound generation and propagation process
- sufficiently high sound pressure levels for frequencies up to 40 kHz (for the Aeroacoustic Windtunnel Braunschweig (AWB))
- spherical wave field within an angle of 61°

2.3 Plasma sound sources

Another approach employs an unsteady energy injection as a sound source. Westphal [9] has designed an amplitude-modulated Tesla-generator, as shown in Fig. 3, achieving 250 W of high frequency power by using generating voltages up to 20 kV at the electrode. The air breaks down by an electrode and the ensuing plasma is induced to vibrate. A common design is an amplitude-modulated Tesla-generator with Tesla-coil and electrode working in resonance. The resonance frequencies lie in the range of 10 MHz to 30 MHz and generate a steady plasma flame in an acoustic sense. Using one or more oscillator tubes the plasma is modulated. The changing of the flame size leads to sound radiation. The plasma flame dimensions are small compared to the wavelengths within the audible domain in order that the plasma source can be considered as a compact source. This kind of source possesses a high potential for an omni-directional loudspeaker. The ozone production from the air breakdown is a significant drawback because ozone is a toxic substance. Higher flame temperature can increase the decay of ozone, but this would also lead to increased thermal fatigue of the tungsten electrode which would then have a reduced lifetime. In addition, the design complexity is being increased to help avoid thermal damage of other components. With in-flow applications the flame can be extinguished or fluctuating, which then can cause oscillations. Consequently, heavy damages at the source can occur. The usage of high voltage requires an enclosure for the electrical components for security aspects. It is recommended to shield in the strong electromagnetic emissions arising from the flame by using a surrounding cage of perforated metal plate. However, this cage might influence the radiated sound field due to reflections and interferences. Furthermore, the influence of the electrical and magnetic fields on the measurement equipment has not been fully examined yet. Boden [3] from DLR Braunschweig makes use of a focused laser pulse, as shown in Fig. 4, to generate ionized air in the area of the focal point. This unsteady energy injection leads to a temporary temperature fluctuation accompanied by a pressure fluctuation, so that sound is emitted. In experiments he verified the point source characteristics and an approximate omni-directional sound radiation. The source frequency spectrum in Fig. 5 shows a broad band distribution in the range of 10 to 100 kHz with a global maximum at 70 kHz. In addition, no disturbing experimental setup in the flow is necessary, but the duration of the pulse is with 20 μ s very short. Moreover, results from in-flow experiments have indicated a moving sound source.

3 SOUND SOURCE CONCEPTS FOR IN-FLOW CALIBRATION

The main focus of the sound source design lies in the array amplitude calibration. This means that an ideal monopole source is not mandatory as long as the sound pressure field is homogenous (for example, a cylindrical wave would be appropriate) and not too directional. The following explanations comprise the design concepts of two different calibration sound sources. Both are based on commercially available electromechanical sound transducers. The injected voltage signal allows arbitrary signal components, for example tonal or broadband signals. Sound generation of this type leaves a margin in the spectral signal structure. For other sources such as aeroacoustic or focused laser pulse this is possible only with tremendous effort. The input voltage is very easy adjustable and measurable, which is important for reproducibility.

3.1 Probe A

As mentioned above, the design concept is based upon the sound field generated by commercially available loudspeakers with their typical focused beam patterns. The sound waves will be reshaped through appropriate wave guides in order to obtain an approximate sound field of a breathing cylinder. Fig. 6 shows a design drawing. The sound field generated by the tweeter (17) in the center of the probe, model Vifa XT 300 k/4 adapted for a frequency range of 1.5 kHz to 40 kHz, is passed through the axially symmetric guide body (1) and (7) towards the radiation opening. The width of the opening, a cylindrical ring, can be varied continuously between 1 and 9.8 mm by using a mechanical adjustor (8), so that experiments can be carried out on the influence of the opening width on the emitted sound. The entire probe is enclosed with the aerodynamic fairings. The rear end provides an opening for mounting the probe. The two surfaces for wave guidance are connected by three rods. The positions are shown in Fig. 7. All are arranged symmetrically to the center line AA. The maximum angle between two rods is 200° in order to achieve undisturbed sound radiation of at least 180° . This direction is the preferred alignment to the microphone array. In order to prevent standing waves the rods are shaped as ellipses.

3.2 Probe B

In the probe B, a ribbon loudspeaker from ELAC [5] is employed. A 0.0006 mm thin ribbon, made from aluminium, forms the membrane and is located in a magnetic field. When an alternate current passes through the membrane it expands and contracts like a breathing cylinder because of the ensuing Lorentz forces. The movement of the membrane is in a direction perpendicular to both the magnetic field lines and to the direction of current. It has been designed for a frequency range up to 50 kHz. The ribbon diameter measures 90 mm and has a height of 15 mm. A metal grid protects the sensitive membrane from damage. Two guiding flanges serve as an impedance adjustment and as a diameter extension so that the aerodynamic fairing can be used for both probes, this is leading to a simplification of the manufacturing process. The complete probe is depicted in Fig. 8. As seen in the picture the abutting edges are joined by a screw connection and the protection grid has a tape interface. One may expect interferences and reflections at this location. The upper and lower edges of the membrane are glued to the loudspeaker and hence there are no free oscillations possible.

Below the upper edge an additional mass of a synthetic resin ring is applied onto the ribbon to suppress partial oscillations. Thus, the membrane design is not symmetric, which may affect the sound field.

3.2.1 Resonant cavities

As a direct consequence of the design the probe possesses a resonant cavity. In wind tunnel applications the flows passes over the cavity, at whose edge flow separation can occur, leading to broadband pressure instabilities. These can induce cavity resonances. A metal grid covered with silk, masking the cavity, reduces the instability excitation, as illustrated in Fig. 9. As a tradeoff, one has to accept the sound wave interferences and reflections at the masking.

4 EXPERIMENTAL SETUP

This chapter describes the experimental setup and the measurement equipment.

4.1 The anechoic chamber

The measurements were conducted in the anechoic chamber of the Institute of Fluid Mechanics and Technical Acoustics (ISTA) at the Technical University of Berlin. The room has a free volume of 1850 m³. The sound absorbing wedges at the walls, floor and ceiling enable free field measurements above a cut-off frequency $f_g=63$ Hz. A steel net with a surface of 16 m x 12 m provides a base area for the experimental setup.

As a support for the experimental setup, a frame made from aluminum profiles is employed, upon which all parts are mounted, as shown in Fig. 10. That ensures fixed distances between various components. The calibration sound sources are mounted vertically on a rotational unit. This unit facilitates the adjustment of arbitrary angles with minimal step size of 0.0375°. The axis of rotation is identical with the probe center-line. Furthermore, a microphone is mounted on an additional traverse for distance variations along the x-axis between source and receiver. The experimental setup can be extended by a second traverse for different z-positions.

4.2 The coordinate system

Two different coordinate systems are employed, cylindrical or Cartesian, the choice being dependent on what is being examined. The coordinate origins coincide with the center point at the center line of the calibration sound sources. This is illustrated in Fig. 6 and 7. The following equations give the transformation from the one coordinate system to the other:

$$\begin{aligned}\gamma &= \sqrt{x^2 + y^2} \\ x &= \gamma \cos \theta \\ y &= \gamma \sin \theta \\ z &= z\end{aligned}\tag{1}$$

At the probe A the coordinate $\theta = 0^\circ$ is located at the center line of one bridge. The remaining two lie at 80° and 160° . In the case of probe B, $\theta = 0^\circ$ is located at the abutting edges of the membrane.

4.3 Test series

The aim of the experiments is to determine the directional characteristics of sound radiation for both sound sources. In the first part the probes rotate step by step, the center of rotation being the z-axis. The microphone position does not alter its position in relation to the anechoic room, but due to the fixed coordinate system regarding the probe the sensor coordinates vary. In the second part θ remains constant and the microphone is traversed along the z-axis.

4.4 Test series overview

For the measurements a calibrated free-field G.R.A.S. $\frac{1}{4}$ " microphone (type 40 BF) was used. Band-pass filtered white noise serves as the loudspeaker input signal and the data acquisition system VIPER-48 from GBM samples the microphone signal at a sampling rate of 140 kHz for the duration of 20s.

4.4.1 Azimuthal directivity

The main focus of this part is the xy-plane. For both probes A and B the listed measurement program in Table.1 is performed. The variations are limited to the angle θ . Pertaining to the design features various parameter studies are conducted. The parameter variations for probe A comprise the opening width (1 mm, 9.8 mm) and its influence on the emitted sound field, while for probe B the masking of the opening with a metal grid and silk is mainly considered.

Table 1. Measurement points for probes A and B for azimuthal directivity.

γ [mm]	z [mm]	θ_{start} [°]	θ_{end} [°]	$\Delta\theta$ [°]
1080	0	0	360	6

4.4.2 Polar directivity

In the second part the sound field along the z-axis is measured and Tables 2 and 3 contain the various parameter settings. Probe design features like rod locations and membrane abutting edges define the application settings.

Table 2. Test series for probe A for polar directivity.

γ [mm]	θ [°]	z_{start} [mm]	z_{end} [mm]	Δz	s [mm]
1080	260	-500	500	25	1 and 9.8

Table 3. Test series for probe B for polar directivity.

γ [mm]	θ [°]	z_{start} [mm]	z_{end} [mm]	Δz
1080	90	-500	500	25
1080	180	-500	500	25

4.5 Synthetic microphone array processing

The measurements were performed with a single microphone at different locations. Afterwards a synthetic microphone array can be arranged combining the single microphone measurements. However, there is a fundamental difference compared with a real phased microphone array, where the signal recording takes place simultaneously. The signal phases have a direct relationship to each other, which is not the case with single microphone measurements. Therefore the injected loudspeaker voltage signal is measured at the same time with the microphone signal. The FOURIER-transformed correlation of both signals yields a frequency dependent complex cross-correlation coefficient $S_{RP}(\omega, \vec{x}_m)$ for each microphone measurement position \vec{x}_m . It contains the frequency dependent phase information about the wave field relative to the input signal, which is needed for beamforming. The term still contains components of frequency dependent phase shifts which are caused by the data acquisition system and the loudspeaker itself and which are independent of the microphone position. The cross-correlation coefficients can be presented as a vector:

$$\vec{S}_s(\omega) = \begin{pmatrix} S_{RP}(\omega, \vec{x}_1) \\ S_{RP}(\omega, \vec{x}_2) \\ \vdots \\ S_{RP}(\omega, \vec{x}_m) \end{pmatrix} \quad (2)$$

Again, by means of the cross-correlation vector one can calculate the synthetic cross-correlation matrix, where $()^H$ denotes the conjugate complex transpose vector.

$$R_s(\omega) = \vec{S}_s \vec{S}_s^H \quad (3)$$

Thereby the phase differences due to the measurement devices are compensated. This approach is feasible since one obtains for the normalized cross-correlation coefficient

$$\left| \frac{S_{RP}}{\sqrt{S_{RR} S_{PP}}} \right| \approx 1 \quad (4)$$

since no noteworthy disturbances affect the measurement in the anechoic chamber. Now the conventional beamformer output is computed by

$$A = w^H R_S w \quad (5)$$

where w denotes the steering vector.

5 EXPERIMENTAL RESULTS

5.1 Probe A

5.1.1 Azimuthal directivity results

Fig. 11 shows the measured sound pressure for the opening width of 1 mm and 9.8 mm plotted over the frequency f and the coordinate θ . The measurement was carried out in the $z = 0$ plane for different θ and the microphone is located 1.08 m away from the point of origin which is identical with the probe center point. The traversing was conducted in 6° steps. Independent of the opening width, the highest amplitudes will be achieved below 20 kHz, whereby, however, with increasing frequency the amplitudes decrease. This is probably due to the original design of the loudspeaker being meant for audio applications optimized for the human audible range. The opening width influences directly the radiated sound. The amplitudes are lower for an opening of 1 mm in comparison with 9.8 mm. The highest level of 58.3 dB is emitted at maximal opening. In fact, that is too low for future wind tunnel applications and in all likelihood the wind tunnel background noise will cover the probe signal. Furthermore the amplitude fluctuations in the spectra depend on the frequency and the coordinate θ . The three bridge positions at $\theta = 0^\circ$, 80° and 160° cannot be identified by means of the spectra. Resonances and standing waves within the probe generate sound pressure fluctuations up to 20 dB by consideration of a narrow frequency band. For the local maxima and minima positions in the θ -plane it is obviously unimportant how big the opening width is. In general the number of minima and maxima increases with rising frequency and the amplitudes decrease.

5.1.2 Polar directivity results

In the following results will be presented for measurements along the z -axis. The microphone was traversed along the z -coordinate and θ varied. That yields varying distances between observer and probe center point so that $1/r$ correction is carried out for amplitude comparisons. The analysis comprises narrow band spectra as depicted in Fig. 12. The plots show the sound pressure levels depending on frequency f and the z -coordinate at $\theta = 260^\circ$. The regarded opening widths constitute 1 and 9.8 mm. The same tendencies as before occur. With rising opening width the amplitude increases. The higher sound pressure levels are accompanied by greater amplitude fluctuations starting at 20 kHz. The probe radiates an asymmetric wave field with respect to $z = 0$. That can be a result of the different nose and tail contours and the asymmetry inside the probe. For both configurations there exists a strong frequency dependence of the amplitudes.

5.1.3 Synthetic microphone array results

The measurements were conducted with a single microphone. Under certain condition one can combine these single measurements to construct a synthetic microphone array which is

illustrated in Fig. 13. It consists of two crossed arms. One of them is located at $\theta = 260^\circ$, which corresponds to the preferred orientation in the calibration process. The 201 microphones are equidistantly distributed and have 5 mm spacings. The second arm consists of 180 sensors positioned in a semicircle in the xy-plane with a distance of $r=1080$ mm from origin. The central microphones form the crossing point of the two arms. The beamforming results in Fig. 14 and 15 are computed on 80000 grid points in the xy-plane, exemplified by a low and a high frequency case. The white circle marks the probe cross section in the observation plane. Besides the calculated source maps for the measured microphone signals source maps of a simulated monopole in the origin were computed. For reasons of comparability the focused powers are normalized so that one obtains $L_{p,fn} = 0$ dB at the maximum. The microphone array exhibits a certain frequency response and cannot resolve the monopole as a point source, as the simulations reveal. The source maps for $f=5007$ Hz match qualitatively in the xy-plane. In comparison with the monopole simulation the focussed level maximum, computed for the measurement data, is shifted about 1 mm in negative x-direction and 2.5 mm in positive y-direction. Moreover, the level differences between the main lobe and the side lobes are greater with the simulation. The differences between the microphone signals and the simulation are greater at higher frequencies. Both source patterns do not correspond to each other. The maximum is shifted again. This time the values are $\Delta x=1$ mm and $\Delta y=1.5$ mm.

5.2 Probe B

5.2.1 Azimuthal directivity results

The f - θ -plots in Fig. 16 show the sound pressure level directivity in the plane $z = 0$ in clean configuration and with grid and silk masking. The highest levels are obtained below 20 kHz as it is sufficiently for audio applications. The amplitude decreases with growing frequency. The abutting edges with the electrodes cause an enormous amplitude reduction, mainly in the range of $\theta=335^\circ$ to $\theta=25^\circ$. The symmetric loudspeaker design is reflected in the symmetric wave field with respect to the line $\theta = 180^\circ$. The measured pressure levels are higher than accomplished with probe A, but future in-flow tests will show if it is sufficiently enough. The masking reduces the emitted sound of the entire spectrum. Starting at 25 kHz many drops in the observed pressure level occur due to interferences generated by the masking.

5.2.2 Polar directivity results

As before for probe A, the analysis comprises the examination of the wave field along the z-axis. For the narrow band spectra a distance compensation is again calculated. The plots in Fig. 17 show the sound pressure level depending on frequency f and the z-coordinate at $\theta=90^\circ$ and $\theta=180^\circ$. Both fields show a similar result. Nevertheless frequency and spatially dependent amplitude decreases can be recognised. Especially in the range of $z = -300$ mm to $z = -500$ mm there are sound pressure level variations for the frequencies between 10 kHz and 20 kHz. An influence of reflections at the traverse or the experimental setup can be excluded because the measurements with the probe A do not show these effects. The probe radiates an asymmetric wave field with respect to $z = 0$, which could be caused by the different nose and tail contours or the slight asymmetric membrane.

5.2.3 Synthetic microphone array results

In Fig. 13 is shown the synthetic microphone array which was used for beamforming in the same manner as for probe A. Again, it consists of two crossed arms, but with a different angle alignment at $\theta=180^\circ$. This arm has 201 microphones distributed equidistantly along a line with 5 mm spacings between the sensors. 180 microphones are distributed in the xy-plane on a semicircular with a distance of $r=1080$ mm from origin. The central microphones again form the crossing point. The approach for computing and plotting the beamforming results is identical with the previous case for probe A. The sources maps in Fig. 18 and Fig. 19 are calculated for the frequencies $f=7998$ Hz and $f=62993$ Hz. The white circle again marks the probe cross section in the observation plane. The simulations serve to provide a comparison with the measurements. The deviations between the source patterns are substantial and it becomes apparent that the sound source is not an ideal monopole. The focussed maximum in the source map for $f=5007$ Hz is shifted about 1 mm in positive x- and y-directions in comparison to the simulated maximum. In the case of $f=62993$ Hz, a deviation for $\Delta x=1$ mm only occurs.

6 COMPARISON OF THE RESULTS

The amplitude response of probe A shows frequency dependent drops. The spatial amplitude fluctuations are not so distinct for an opening width of 1 mm as for 9.8 mm. As a tradeoff, the emitted pressure levels are smaller for a width of 1 mm. Neither the amplitude response nor the phase response reveals a monopole directivity. In terms of the amplitude response, probe B exhibits at least partially monopole characteristics in the xy-plane and radiates higher pressure amplitudes compared to probe A. In addition, the phase response differs less from an omni-directional sound source than for the other calibration sound source. The probe B fulfils more requirements for a microphone array calibration source.

7 SUMMARY

The present study reviews concepts for omni-directional sound sources and evaluates their capability for microphone array calibration. Two concepts of calibration sources with aerodynamic fairings have been developed. The radiated sound field of both probes was examined in experiments in a class I anechoic facility. The presented results comprise the spatial amplitude characteristics of the designed sound sources. In addition, beamforming with a synthetic microphone array was performed to analyse the phase characteristics.

In future in-flow tests with the calibration sound source in a closed test section, the quality of the aerodynamic fairings and the practicability in aeroacoustic testing will be examined.

REFERENCES

- [1] Bang & Olufsen, <http://www.bang-olufsen.com>.
- [2] Brüel & Kjaer, <http://www.bksv.com>.
- [3] F. Boden, "Entwicklung einer neuartigen Laserschallquelle", DAGA, 2006.

- [4] W. Dobrzynski, K. Nagakura, B. Gehlhar, A. Buschbaum, “*Airframe Noise Studies on Wings with Deployed High-Lift Devices*”, 4th AIAA/CEAS Aeroacoustics Conference, AIAA-Paper 1998-2337, Toulouse, France, 1998
- [5] ELAC, <http://www.elac.de>.
- [6] A. Lauterbach, “*Wechselwirkungen von akustischen Wellen mit turbulenten*
- [7] *Strukturen in Windkanalschichtungen*”, diploma thesis, Georg – August University Göttingen, III. Physical Institute, 2006
- [8] MBL, <http://www.mbl-germany.de>.
- [9] T.J. Mueller, “*Aeroacoustic Measurements*”, Springer Verlag, 1. Auflage, 2002
- [10] H. Westphal, *personal talk and presentation of the plasma loudspeaker developed by Tigris Company and Technical University of Berlin*, <http://www.tigris.de>, 2007



Fig. 1. Loudspeakers from Bang & Olufsen [1], MBL [7] and B & K [2].

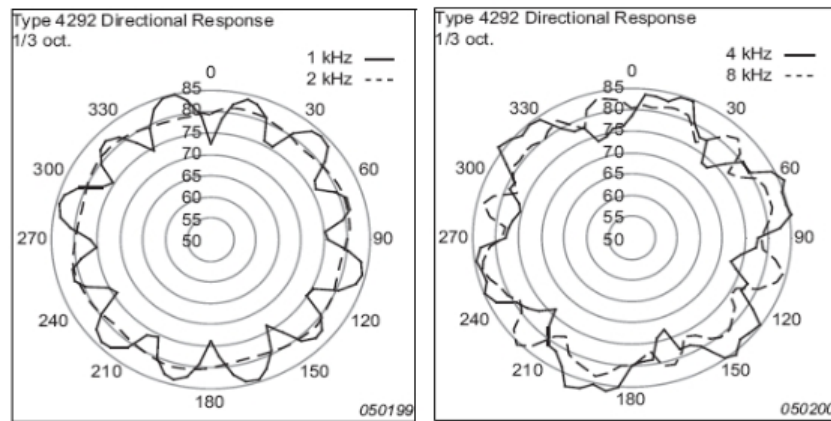


Fig.2. Sound field directivity from B & K source 4295.

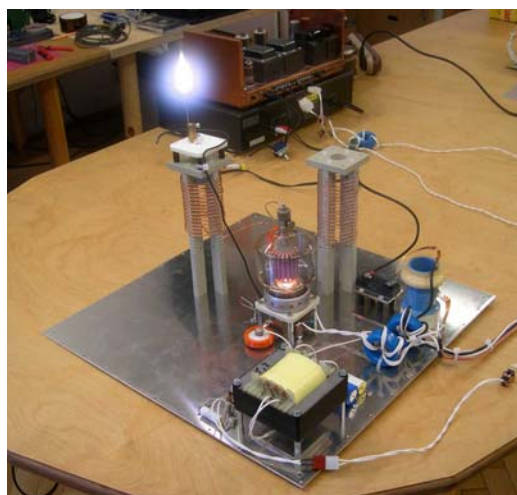


Fig.3. Plasma loudspeaker from Westphal [9]

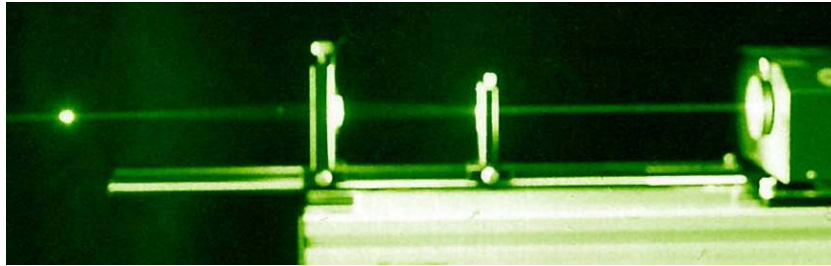


Fig.4. Focussed laser pulse as sound source from Boden [3].

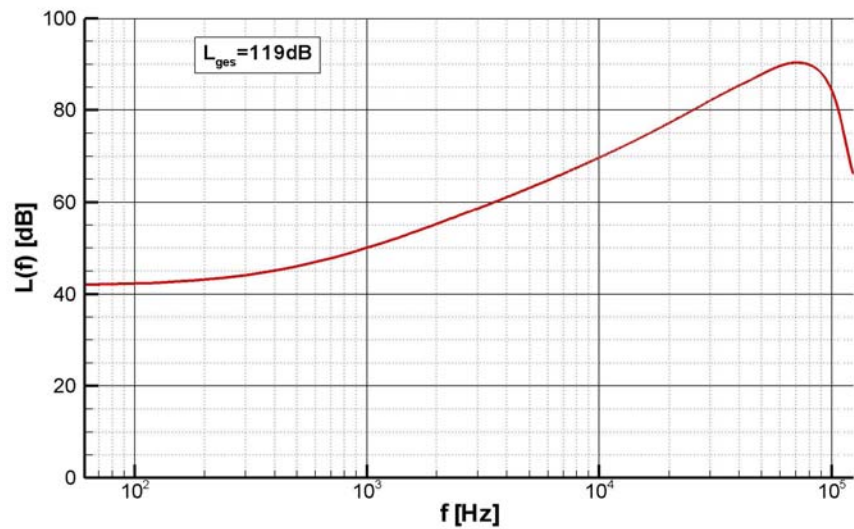


Fig.5. Frequency spectrum from the focused laser pulse measured 200 mm away from the pulse without flow from Boden [3].

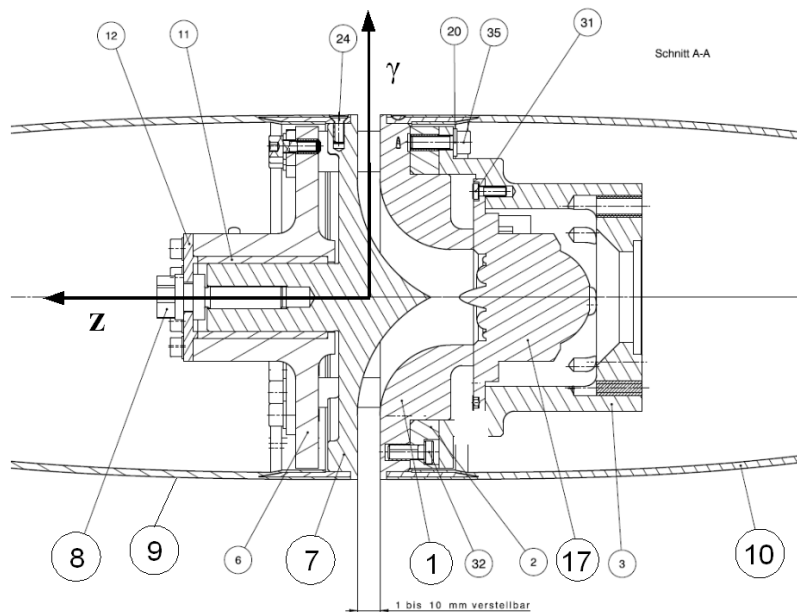


Fig. 6. Design drawing and coordinate system of probe A.

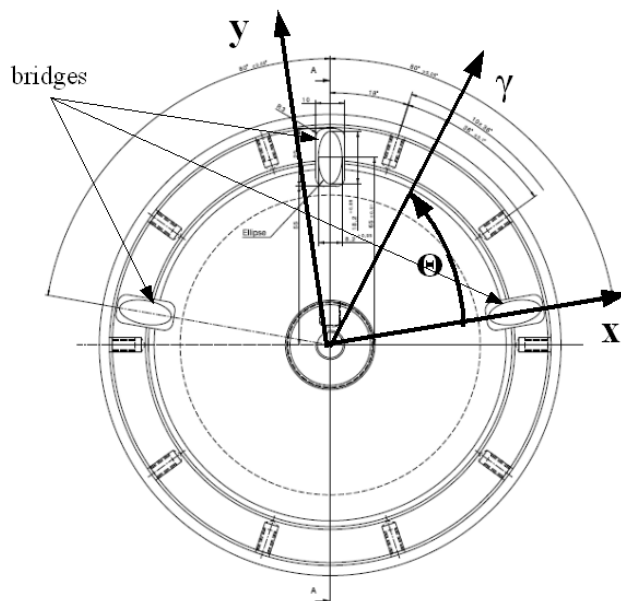


Fig. 7. Rods from probe A and coordinate system of probe A.

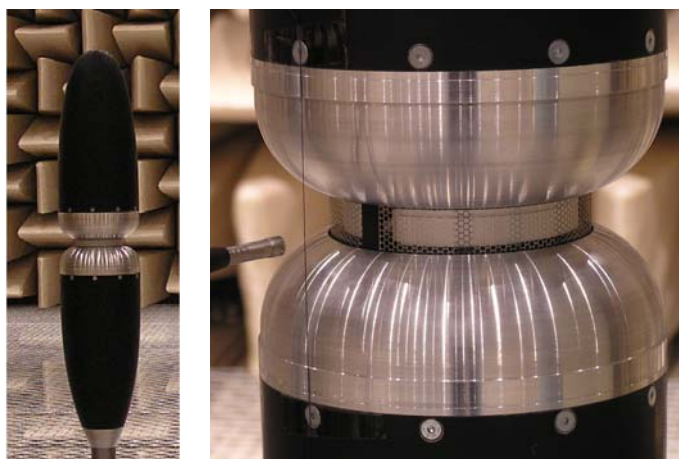


Fig. 8. Probe B with its ribbon membrane and with original grid for protection.

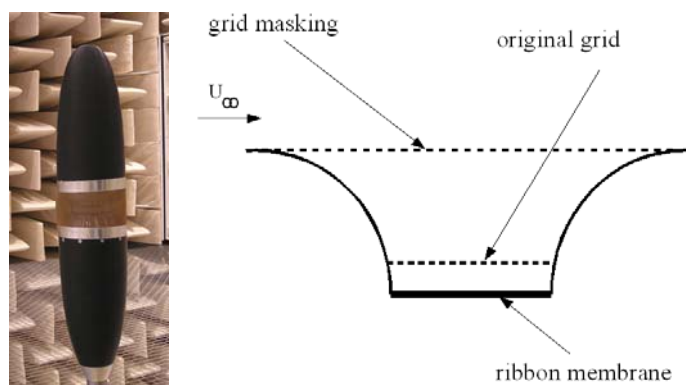


Fig. 9. Probe B with masking and schematic sketch of the cavity masked with a grid.

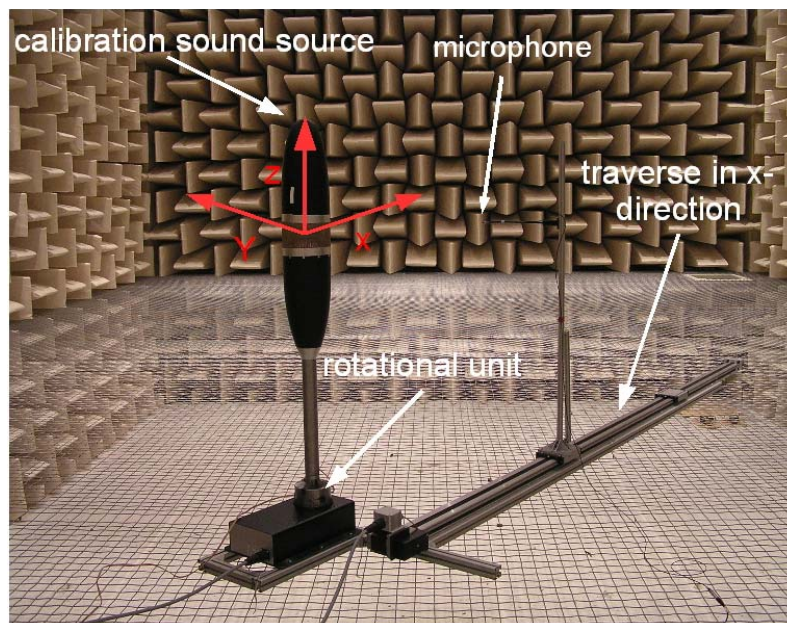


Fig. 10. Experimental setup in the anechoic facility of ISTA.

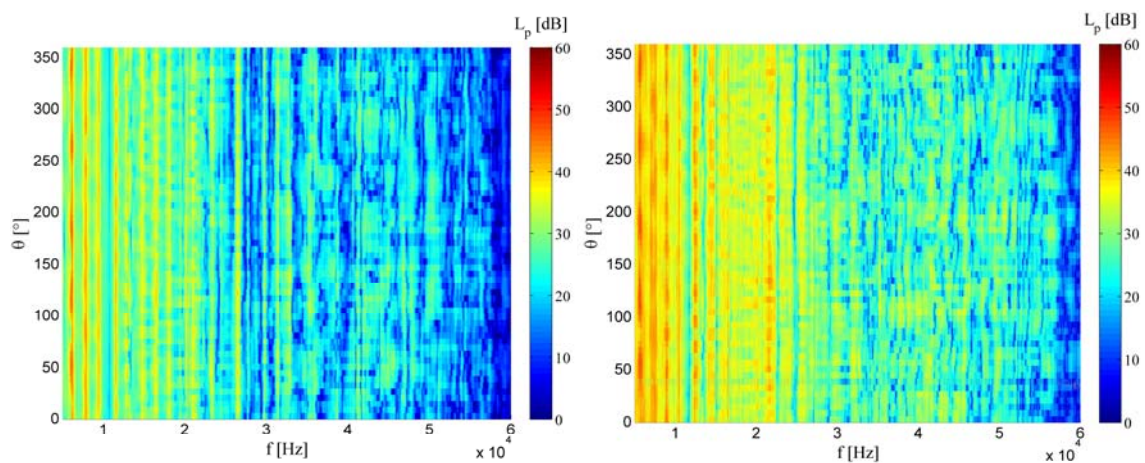


Fig. 11. Measured pressure level from probe A as function of θ for opening width 1.0 mm (left) and 9.8 mm (right).

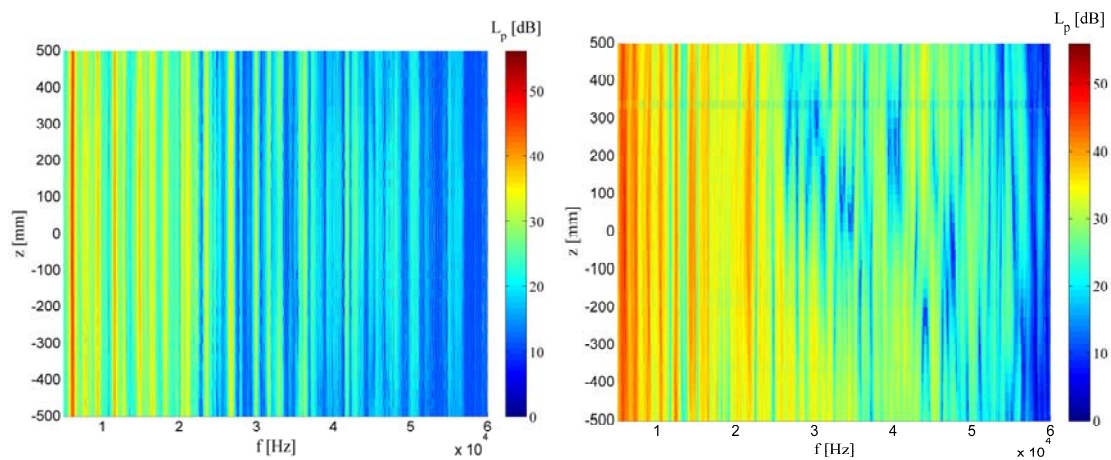


Fig. 12. Measured pressure level from probe A as function of z and $\theta = 260^\circ$ for opening width 1.0 mm (left) and 9.8 mm (right).

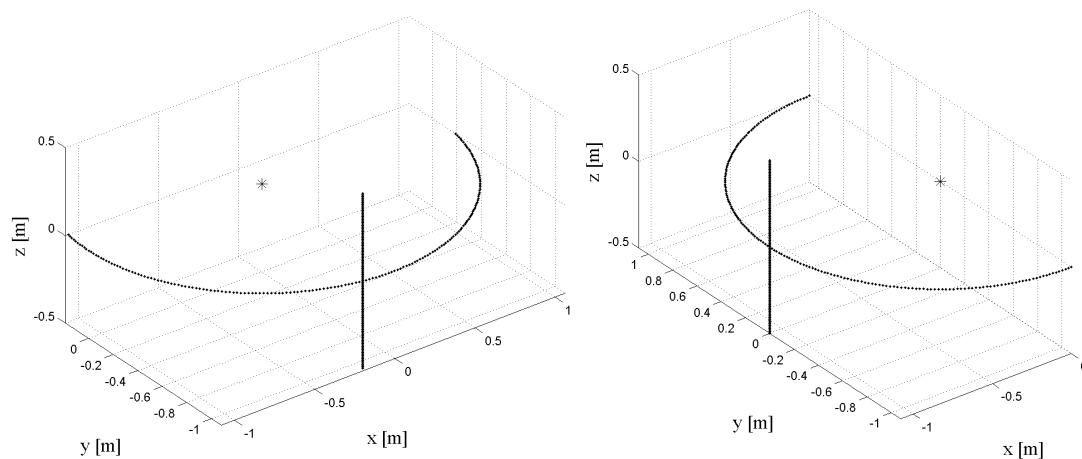


Fig. 13. Synthetic microphone array for probe A (left) and probe B (right).

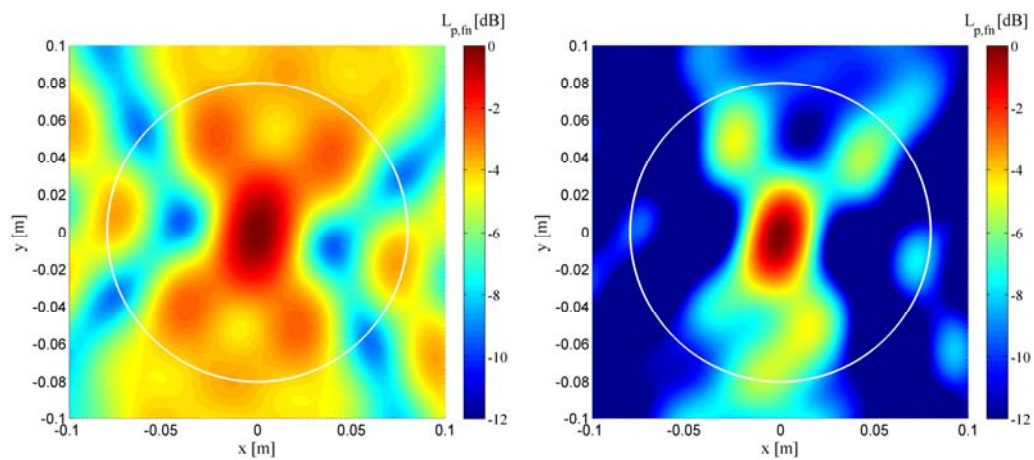


Fig. 14. Beamforming results of probe A for $f=5007$ Hz for simulated monopole (left) and measurement (right).

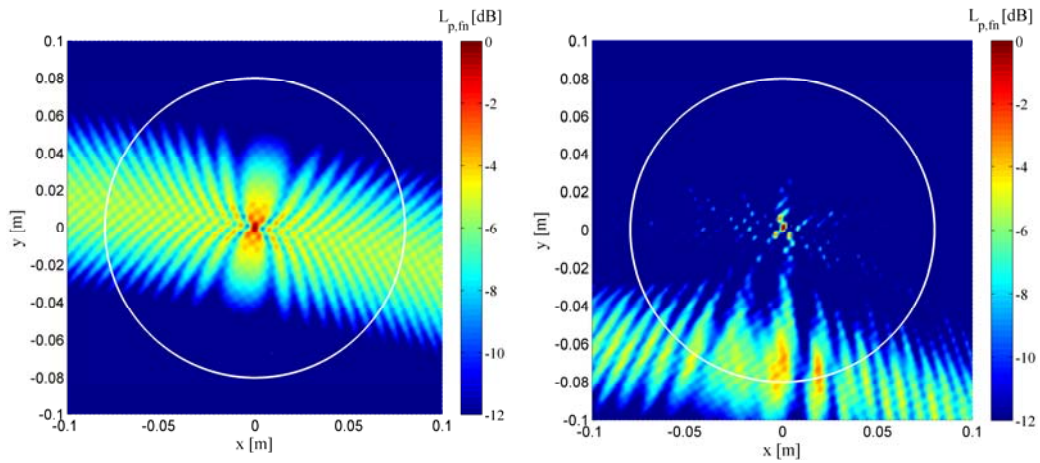


Fig. 15. Beamforming results of probe A for $f=50005$ Hz for simulated monopole (left) and measurement (right).

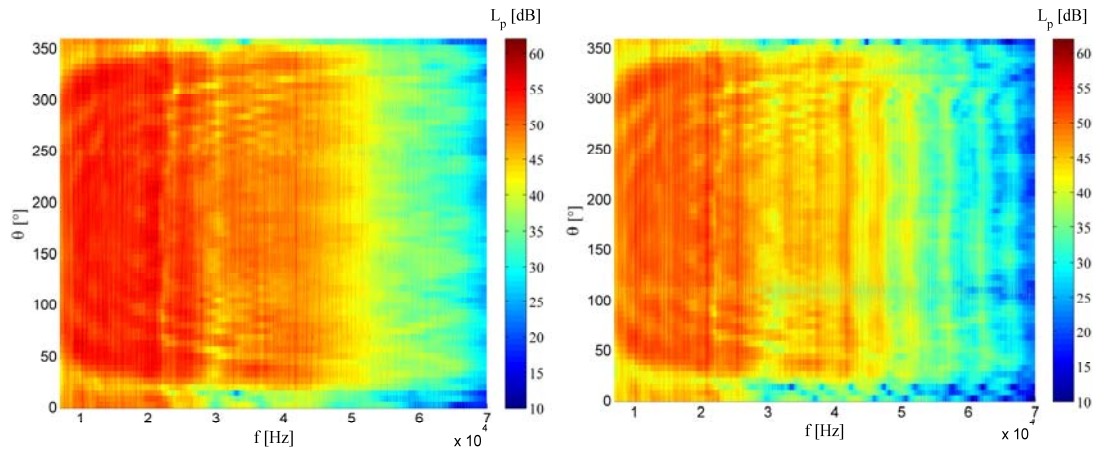


Fig. 16. Measured pressure level from probe B as function of θ for the clean configuration (left) and with grid and silk masking (right).

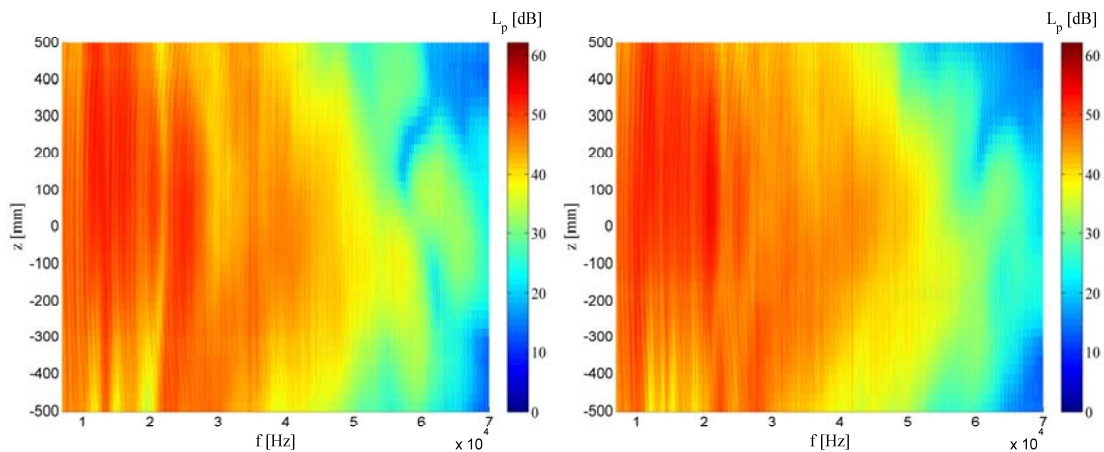


Fig. 17. Measured pressure level from probe B as function of z for $\theta=90^\circ$ (left) and $\theta=180^\circ$ (right).

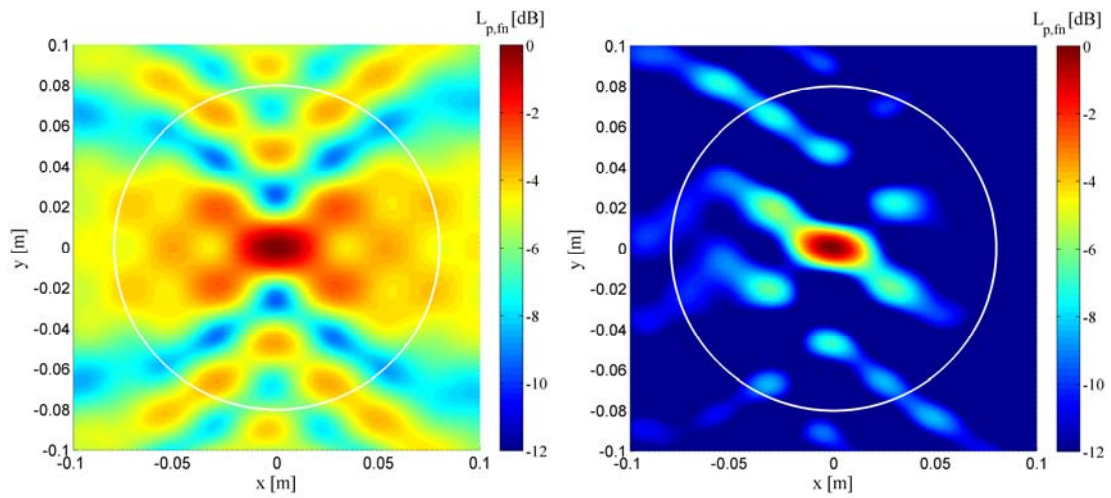


Fig. 18. Beamforming results of probe B for $f=7998$ Hz for simulated monopole (left) and measurement (right).

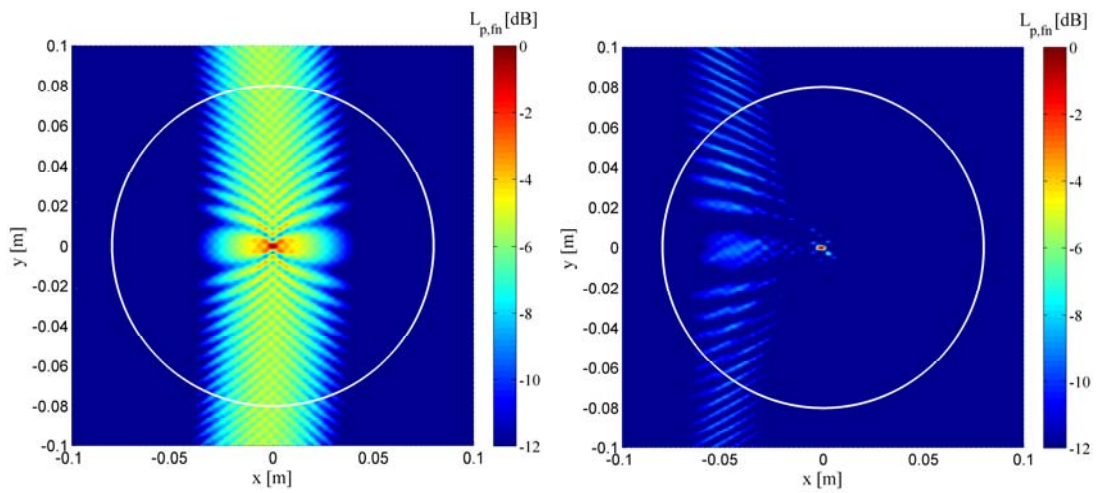


Fig. 19. Beamforming results of probe B for $f=62993$ Hz for simulated monopole (left) and measurement (right).